Materials Advances

ROYAL SOCIETY OF CHEMISTRY

PAPER

View Article Online
View Journal | View Issue

Cite this: *Mater. Adv.*, 2024, 5, 3881

Mechanochemically-assisted synthesis of 3D, 2D and quasi 2D lead halide perovskites for supercapacitor applications†

Apurba Mahapatra, *[a] Manoranjan Mandal,[b] Ayon Das Mahapatra,[c] Vishnu Anilkumar,[a] Jan Nawrocki,[a] Rohit D. Chavan,[a] Pankaj Yadav*[d] and Daniel Prochowicz *[a]

Lead halide perovskite (LHP) thin-film-based energy storage devices have gained considerable attention due to their favourable electronic and ionic conductivity. Here, we have fabricated electrodes for electrolyte-based supercapacitors using mechanochemically synthesized LHPs and demonstrated that the type of starting material and dimensionality of the perovskite strongly influence the device performance. First, we have compared the electrochemical performance of electrodes obtained from the single crystalline (SCP) and mechanosynthesized (MSP) methylammonium lead tribromide ($MAPbBr_3$), and ~2 times improvement was observed in the $MAPbBr_3$ MSP-based energy storage device due to higher average microstrain induced by ball milling, which modulates ion migration. Next, we fabricated electrodes based on mechanochemically synthesized $MAPbBr_3$, 2D MA_2PbBr_4 and quasi-2D $BA_2MAPb_2Br_7$, and demonstrated that the structure and ion migration could play a vital role in the overall performance of the LHP-based electrochemical supercapacitor. The areal capacitance (~209 mF cm^{-2}) and specific capacitance (~138.35 F g^{-1}) calculated at a scan rate of 5 mV s^{-1} with the maximum power density and cycle stability were found to be highest in the 2D MA_2PbBr_4 perovskite-based supercapacitor. This result can be attributed to its smallest particle size, which helps to improve the interaction between electrolyte ions and the perovskite electrode interface at a lower scan rate.

Received 18th December 2023,
Accepted 28th February 2024

DOI: 10.1039/d3ma01144e

rsc.li/materials-advances

1. Introduction

The utilisation of green energy generated from solar cells may be limited due to its intermittent nature and weather-dependent performance. Thus, energy storage is essential to store the energy generated from solar cells at their peak performance and utilise the stored energy during the night or in bad weather. On the other hand, innovative energy storage devices with low cost and efficient performance are also vastly desirable to fulfil the growing demand for renewable power grids and electric vehicles. Electrochemical batteries are majorly used energy storage devices for uninterrupted energy supply. Supercapacitors (SUCs) are an attractive alternative to electrochemical batteries because of their high power density and long cycle life.[1,2] Therefore, many efforts have been made to solve the relatively low energy density problem of SUCs to reach the industrial benchmark standards for a wide-range of applications such as electric vehicles, various electronic devices, and pulse power systems.[1]

Lead halide perovskites (LHPs) are widely used for the fabrication of high-efficiency photovoltaic cells and other opto-electronic devices such as LEDs, sensors, and photodetectors.[3–7] Recently, LHPs have been extensively explored as SUC working materials due to their high ion diffusion and mixed conductivity properties.[8–11] Ions in the LHPs have low activation energies with significant ionic diffusion coefficients, which are favourable properties for efficient SUCs. In addition, easy and cost-effective fabrication of LHP materials with desired high ionic conductivity attracts the research community as emerging candidates for SUC application.[11–13] Electrochemical supercapacitors (ESCs) typically consist of two narrow distanced electrodes filled with the electrolyte.[13,14] The porosity of the electrodes increases the effective surface area with the electrolyte, and increases the ionic diffusion at the electrode/electrolyte interface. For this reason., the ion migration issue of LHP materials is a reward for ESC application.[15]

[a] *Institute of Physical Chemistry, Polish Academy of Sciences, Kasprzaka 44/52, Warsaw 01-224, Poland. E-mail: amahapatra@ichf.edu.pl, pankaj.yadav@sse.pdpu.ac.in, dprochowicz@ichf.edu.pl*
[b] *Department of Physics, School of Science, GITAM University, Bengaluru, 561203, India*
[c] *Institute of Chemistry, Hebrew University of Jerusalem, Jerusalem, 9190401, Israel*
[d] *Department of Solar Energy, School of Energy Technology, Pandit Deendayal Energy University, Gandhinagar, 382 007, Gujarat, India*

† Electronic supplementary information (ESI) available. See DOI: https://doi.org/10.1039/d3ma01144e

LHPs can be used as either a cathode or an anode, or both in the ESCs. Zhou *et al.* first explored the use of an LHP as an electrode material in an electrochemical capacitor by utilising the ionic conduction of methylammonium lead triiodide ($MAPbI_3$).[16] Generally, the electrochemical performance of the electrode materials is directly related to the morphology and their synthesis technique. For instance, Bag *et al.* reported porous electrodes from $MAPbBr_3$ single crystals (SCs) with an areal capacitance of 81.5 mF cm^{-2} at a fixed current density of 5 mA cm^{-2} as compared to 39.8 μF cm^{-2} for $MAPbBr_3$ thin-films.[9] On the other hand, the spark plasma sintering chamber processed $MAPbI_3$ powder-based solid-state pellet SUC devices show ultrahigh energy density (34.2 W h kg^{-1} at 100 Hz). Therefore, the synthesis protocol of LHPs strongly influenced the performance of LHP-based ESCs. Recently, photorechargeable SUCs have been demonstrated by using $MAPbBr_3$ SC-based porous electrodes that can simultaneously harvest solar energy and store it.[17]

In this work, we reported for the first time the fabrication process of electrodes for supercapacitors from the mechanochemically synthesized LHPs. First, we compared the structural and morphological properties of $MAPbBr_3$ synthesized by high-energy ball milling of perovskite precursors (denoted as $MAPbBr_3$ MSP) and grinding $MAPbBr_3$ single crystals (denoted as $MAPbBr_3$ SCP). The XRD structural analysis of $MAPbBr_3$ MSP shows the presence of higher microstrains compared to the $MAPbBr_3$ SC. These microstrains and applied synthesis protocol for electrode formation highly influence the ion migration in these materials. We have utilized both materials as potential active electrodes. The electrochemical capacitor measurements show a maximum specific capacitance of ~159 mF cm^{-2}/98.36 F g^{-1} at a scan rate of 5 mV s^{-1} for the $MAPbBr_3$ MSP-based electrode, which is much higher than that of all reported $MAPbBr_3$-based ESCs, and surpass all existing $MAPbBr_3$-based electrode's capacitance with the same electrolyte and device structure.[9,18] Next, we investigated the effect of structural evolution on the total capacitance of LHP-based supercapacitors by testing 3D $MAPbBr_3$, 2D BA_2PbBr_4 and quasi-2D $BA_2MAPb_2Br_7$. It is found that the 2D MA_2PbBr_4 MSP-based electrode shows maximum areal capacitance (~209 mF cm^{-2}) and specific capacitance (~138.35 F g^{-1}) at a scan rate of 5 mV s^{-1}, besides having relatively slower and lower ion kinetics compared to the other samples. This is due to the smallest particle size of the BA_2PbBr_4 MSP as compared to the other MSPs, which improves the interaction between electrolyte ions and increases the effective surface area in the perovskite electrode interface. Stability analysis of these devices was also carried out over 2000 cycles of charging and discharging. Among the studied materials, the 2D BA_2PbBr_4 MSP based supercapacitor retains over 97% capacitance and shows maximum stability due to the slowest ion kinetics.

2. Experimental section

2.1. Synthesis of single crystalline and mechanosynthesized LHP powders (MSPs)

$MAPbBr_3$ single crystals (SCs) were synthesised using the inverse temperature crystallisation (ITC) method.[19,20] 1.2 M $MAPbBr_3$ solution was prepared by dissolving equimolar amount of lead(II) bromide ($PbBr_2$) and methylammonium bromide (MABr) in dimethylformamide (DMF) and stirred for 4 h at room temperature. Next, the solution was filtered using a 0.2 μm PTFE filter and kept at 85 °C in a sealed bottle for 3 h, which resulted in the growth of $MAPbBr_3$ SCs. The $MAPbBr_3$ SCs were ground for 40 min in a Retsch MM200 mill at 30 Hz to prepare $MAPbBr_3$ SC based powder (SCP). All LHP MSPs were synthesised in a solid-state high-energy ball mill in a similar way (ground for 40 min at 30 Hz). For $MAPbBr_3$, MABr and $PbBr_2$ and for BA_2PbBr_4, benzylammonium bromide (BABr) and $PbBr_2$ were taken as starting precursors. Stochiometric proportions of these starting precursors were taken in an airtight vial and mixed in a Retsch MM200 mill at 30 Hz for 40 min. For the mechanosynthesis of $BA_2MAPb_2Br_7$, the as-prepared $MAPbBr_3$ and BA_2PbBr_4 were mixed in 1 : 1 molar ratio and ground using a similar procedure.

2.2. Material characterization

All obtained halide perovskite powders were characterized using an Empyrean X-ray powder diffractometer (PANalytical) with Cu Kα radiation (λ = 1.5406 Å) over a 2θ range of 10° to 50° at room temperature. The operating current and voltage were kept at 40 kV and 40 mA, respectively. Morphological analysis of perovskite powders was performed using an FEI Nova NanoSEM 450 scanning electron microscope under high vacuum.

2.3. Electrode preparation and electrochemical characterization

The electrochemical experiments were characterized with a BioLogic SP-150 potentiostat by using the standard three-electrode technique in a small-volume analytical cell. For supercapacitor measurements, LHP powders were used as the working electrodes, the Pt metal was used as the counter electrode and the Ag/AgCl was used as the reference electrode. 0.1 M tetrabutylammonium tetrafluoroborate ($C_{16}H_{36}BF_4N$) in dichloromethane solvent is used as the liquid electrolyte.[9] LHP based electrodes were prepared by drop casting a LHP slurry on a glassy carbon electrode (diameter = 3 mm) and dried at 70 °C for 12 h in an air oven. The homogeneous slurry of LHPs was prepared by mixing 80 wt% of the synthesized perovskite powder, 10 wt% of polyvinylidene fluoride (PVDF) binder, and 10 wt% of activated carbon in an appropriate amount of NMP solvent for 24 h.

3. Results and discussion

A schematic illustration of the fabrication method of electrodes is shown in Fig. 1. This method involves the use of LHPs obtained from the crystallization process and ball milling of solid starting reagents. Previously, we have shown that the mechanochemically synthesized perovskite powders can be effectively used as an absorber layer in solar cells.[21–24]

Fig. 2a shows pXRD patterns of all the synthesised LHPs by ball milling. The pXRD patterns of the $MAPbBr_3$ SCP and

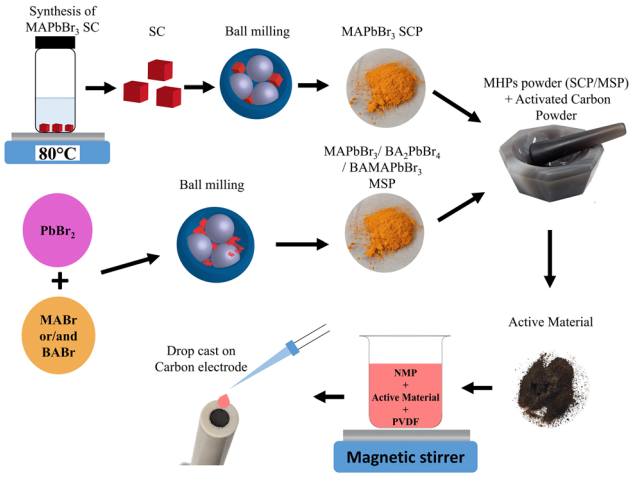

Fig. 1 A schematic illustration of the electrode fabrication based on single crystalline (SCP) and mechanosynthesized $MAPbBr_3$ powders (MSP) for supercapacitor application.

$MAPbBr_3$ MSP show similar diffraction peaks at 2θ = 14.99, 21.21, 30.18, 33.85, and 45.94° assigned to (100), (110), (200), (210) and (300) planes, which confirmed the formation of the pure cubic $MAPbBr_3$ phase.[25] For 2D BA_2PbBr_4, the presence of peaks at 6.44, 12.91, 19.36, 25.86, 32.50, and 39.18° assigned to (002), (004), (006), (008), (0010), and (0012) planes confirmed the formation of the pure 2D orthorhombic crystal phase.[26] The XRD pattern of the quasi-2D $BA_2MAPb_2Br_7$ ($n = 2$) powder shows distinct peaks at a regular interval with a periodicity and preferential orientation along the (0k0) plane confirmed the formation of the pure quasi-2D Ruddlesden–Popper Perovskite (RPP) phase.[27,28] As was previously reported,[9,29] the lattice strain and crystallite size can affect the ion migration in LHP materials. Therefore, we have calculated the microstrain induced on the identical crystallography planes for $MAPbBr_3$ SCP and MSP using the Williamson–Hall (W–H) equation:

$$\beta \cos\theta = 4\varepsilon \sin\theta + \frac{0.9\lambda}{D} \quad (1)$$

where β is the full width at half maximum (FWHM) of X-ray diffraction peaks, ε is the average strain-induced in the materials, λ is the wavelength of X-ray radiation, θ is the position of the diffraction peaks, and D is the average crystallites size. As seen in Fig. 2b, the $MAPbBr_3$ SCP and MSP show different average microstrains of 4.35×10^{-4} and 13.2×10^{-4}, respectively. The higher value of the $MAPbBr_3$ MSP indicates higher lattice distortion introduced during the solvent-free mechanosynthesis process of the perovskite particles, which can modulate the ion migration.[9,29] SEM images of $MAPbBr_3$ SCP and $MAPbBr_3$ MSP are shown in Fig. 2c and d. The particle size distribution of $MAPbBr_3$ MSP is smaller than that of $MAPbBr_3$ SCP sample due to higher strain induced by solvent-free ball milling. These results are in good agreement with the XRD results shown in Fig. 2b. Fig. S1a and b (ESI†) show an SEM image of BA_2PbBr_4 (2D) and $BA_2MAPb_2Br_7$ (quasi-2D) MSP, respectively. It can be demonstrated that the 2D MSP has uniformly distributed spherical shaped micro size morphology

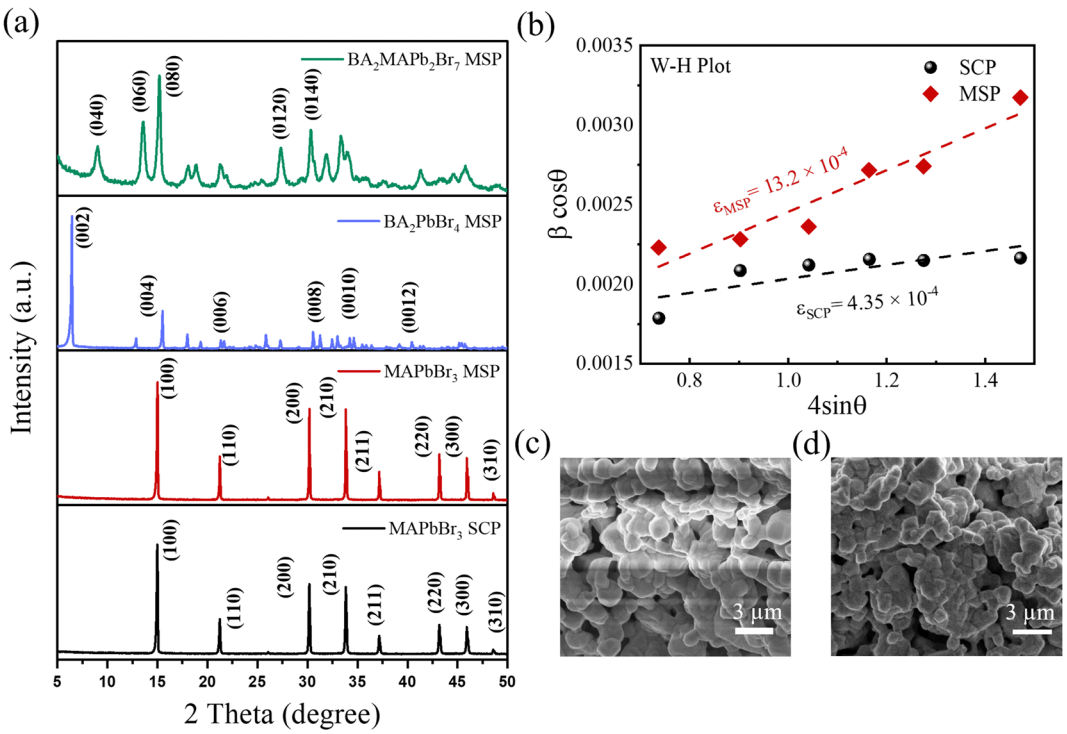

Fig. 2 (a) XRD pattern of $MAPbBr_3$ SCP, $MAPbBr_3$ MSP, BA_2PbBr_4 MSP and $BA_2MAPb_2Br_7$ MSP. (b) A Williamson–Hall plot for $MAPbBr_3$ SCP and MSP. SEM images of the synthesised (c) $MAPbBr_3$ SCP and (d) $MAPbBr_3$ MSP.

with the smallest particle size as compared to the $MAPbBr_3$ (3D) and $BA_2MAPb_2Br_7$ (quasi-2D) MSP.

The electrochemical performance of the fabricated bromide-based materials ($MAPbBr_3$ SCP, $MAPbBr_3$ MSP, BA_2PbBr_4 MSP, and $BA_2MAPb_2Br_7$ MSP) was investigated by measuring their specific capacitance. Cyclic voltammetry (CV), galvanometric charge–discharge (GCD), and electrochemical impedance spectroscopy (EIS) were performed using three electrode systems in 0.1 M $C_{16}H_{36}BF_4N$ electrolyte solution. The specific capacitance of the prepared material is evaluated using the following equations:

$$C_A = \frac{\int I\,dV}{v \times \Delta V \times A} \quad (2)$$

$$C_A = \frac{2I \times \int V\,dt}{A \times \Delta V^2} \quad (3)$$

where eqn (2) represents the areal capacitance from CV measurement, eqn (3) shows the areal capacitance from GCD measurement, $\int I\,dV$ is the integrated area under the CV curve, A is defined as sample deposited area (cm^2), I is the current density, v is the scan rate, ΔV is the potential window (V) and dt is defined as change in discharge time.

The corresponding coulombic efficiency (η, %) was calculated using charging (t_c) and discharging (t_d) times of the GCD using the following relationship:

$$\eta\,(\%) = \frac{t_d}{t_c} \times 100\% \quad (4)$$

Moreover, areal energy density (E_A, W h cm^{-2}) was evaluated using the equation:

$$E_A = \frac{1}{2} \times C_A \times \frac{\Delta V^2}{3600} \quad (5)$$

whereas, areal power density (P_A, W cm^{-2}) was measured using the equation:

$$P_A = \frac{E_A}{t_d} \times 3600 \quad (6)$$

The CV measurements of all the electrodes were conducted at various scan rates ranging from 5 to 120 mV s^{-1} (Fig. S2, ESI†). All the CV spectra exhibit a high degree of symmetry between the charging and discharging sweep without any noticeable redox peak at each scan rate. Therefore, all the electrochemical cells behave as electric double-layer capacitance, and symmetry between charging and discharging sweep suggests fast and efficient electrolytic ion transport into the active pores of all the LHP based electrodes.[8,9,30] The quasi-rectangular shaped CVs of all the ESCs indicate that there is charge contribution from the faradaic mechanism, which is attributed to the diffusion-limited intercalation/de-intercalation process of ions of the liquid electrolyte.[31] Fig. 3a and b show the CV spectra of $MAPbBr_3$ SCP and $MAPbBr_3$ MSP at a scan rate of 5 mV s^{-1}. The $MAPbBr_3$ MSP-based electrode offers a broader integrated CV area than that of the $MAPbBr_3$ SCP electrode, which can lead to a better storage capacity. The maximum areal/specific capacitance values for $MAPbBr_3$ SCP is 75 mF cm^{-2}/50.22 F g^{-1} at a scan rate of 5 mV s^{-1}, which are in the same order as the previously reported work (Table S1, ESI†).[9] In turn, the maximum areal/specific capacitance values for the $MAPbBr_3$ MSP based electrode is 159 mF cm^{-2}/98.36 F g^{-1} at a scan rate of 5 mV s^{-1}, which is almost two times higher than that of the all reported $MAPbBr_3$ based ESCs. The areal capacitance of the electrodes at different scan rates has been evaluated from the CV curves and is plotted as shown in Fig. 3c. The plot shows that the areal capacitance gradually decreases with an increase in the scan rate from 5 to 120 mV s^{-1}. The decrease in capacitance values of respective electrodes is due to ineffective interaction at the interface between the electrolyte ions and perovskite electrode. At a fast scan rate, electrolyte ions do not have sufficient time to diffuse inside the electrode, and only a few ions can access the electrode surface leading to low values in capacitance. The charge storage mechanism of the electrode was further investigated using the Dunn power law: $i_p = a\upsilon^b$. Here, i_p is the cathodic peak current density at a particular potential (*vs.* Ag/AgCl), υ is the scan rate, and the b value signifies the exponent adjustment parameter. If the b value is 1 then it signifies contributions from fast near-surface activities like surface redox reactions and charging/discharging of electric double layer capacitance at the electrode–electrolyte interface and/or faradaic charge transfer at the surface-bound atoms (pseudocapacitance), while the b value of 0.5 represents slow diffusion-controlled faradaic processes (intercalated pseudocapacitance), which involves bulk properties also like a battery (Fig. S3, ESI†).[8] The values of b for $MAPbBr_3$ SCP vary between $\sim$0.98 and 0.77 in the applied potential range of 0.1 to 0.9 V, indicative of a capacitive dominant charge storage mechanism, whereas above 0.9 V and up to 1.1 V, the diffusion contribution surpasses the capacitive contribution part. However, for $MAPbBr_3$ MSP, the b value mostly lies close to $\sim$0.75 in the applied potential range of 0.2 to 0.8 V, which signifies the similar contribution of diffusion and capacitive behaviour of charge storage mechanism. Elsewhere, in the potential window of 0.1–1.1 V, the lower b value ($<$0.7 V) is related to the diffusion mechanism in the corresponding charge storage process. Both $MAPbBr_3$ SCP and $MAPbBr_3$ MSP show transitional behaviour of energy storage (as the b value varies in between 0.5 and 1), where the energy storage process of $MAPbBr_3$ SCP is mostly representative of a surface dominated capacitive process but equal contribution from diffusion-controlled intercalation and surface-capacitive processes is observed for $MAPbBr_3$ MSP. Around a low applied potential range of 0.2–0.3 V, $MAPbBr_3$ SCP acts as a pseudocapacitor and at high potential ($\sim$1.1 V) $MAPbBr_3$ MSP acts like a battery type material.[32] Fig. 3d and e show the GCD graphs of $MAPbBr_3$ SCP and MSP-based electrodes at various scan rates ranging from 0.2 to 0.6 mA cm^{-2}, respectively. The areal/specific capacitances are 67 mF cm^{-2}/44.86 F g^{-1} for $MAPbBr_3$ SCP and 143 mF cm^{-2}/86.66 F g^{-1} for $MAPbBr_3$ MSP at 0.2 mA cm^{-2}. The capacitance values extracted from the GCD are consistent with the CV findings, which reveals the excellent storage capacity of the respective electrode and validate our results. The variation of areal and specific capacitances with different current densities is shown in Fig. 3f. The areal and specific capacitances decrease with an increase in the current density due to the change in the internal resistance of both electrodes. Long-term charging

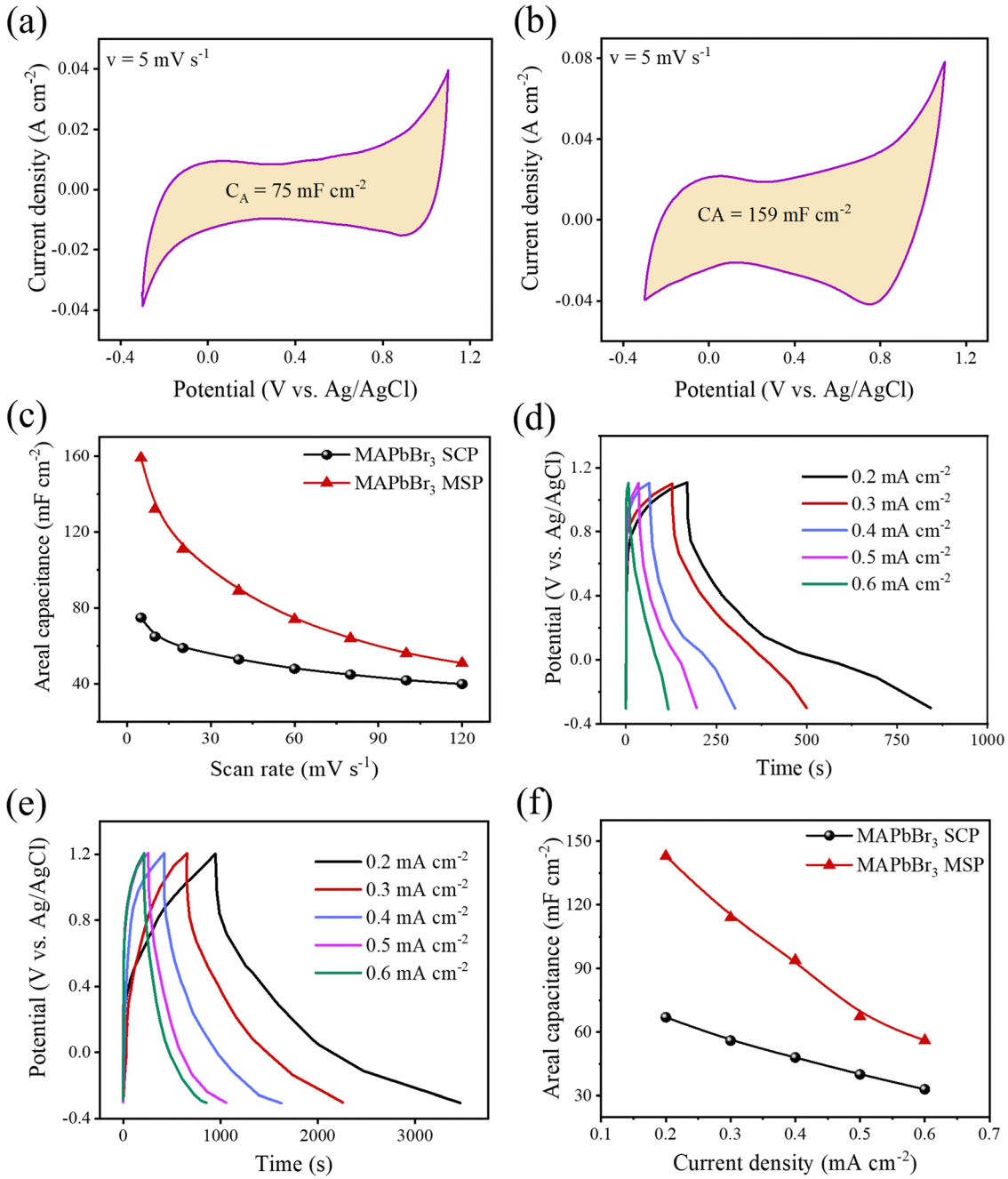

Fig. 3 CV curves at a scan rate of 5 mV s^{-1} for the electrochemical cell based on the (a) $MAPbBr_3$ SCP and (b) $MAPbBr_3$ MSP electrode. (c) Areal capacitance of both electrodes as a function of scan rate in the range of 5 to 120 mV s^{-1}. GCD curves of the (d) $MAPbBr_3$ SCP and (e) $MAPbBr_3$ MSP electrodes at different current densities (0.2–0.6 mA cm^{-2}). (f) Areal capacitance of both electrodes at different current densities.

discharging cycling stability is one of the key parameters for energy storage applications. The long-term cycling stability of both electrodes was evaluated by repeating the GCD measurement for 2000 cycles over a current density of 0.6 A cm^{-2} (Fig. S4, ESI†) within the potential window of 1.5 V. The stability performance of the $MAPbBr_3$ SCP electrode is found to be ~95% capacitance retention, whereas the capacitance retention is around ~93% of its initial capacitance value for the $MAPbBr_3$ MSP electrode. The $MAPbBr_3$ SCP based electrode is more stable compared to the $MAPbBr_3$ MSP based electrode, which can be attributed to the ion migration in metal halide perovskite materials.[8,33] The lattice defects and crystallite size affect the ion migration in metal halide perovskite materials. From the W–H plot (Fig. 1b), we clearly see that $MAPbBr_3$ SCP and $MAPbBr_3$ MSP have different crystallite sizes and microstrain, which can influence the ion migration. Corresponding changes in E_A with P_A for $MAPbBr_3$ SCP and $MAPbBr_3$ MSP are shown in Fig. S5 (ESI†), where the decrement of E_A (from ~0.015 to ~0.009 mW h cm^{-2} for SCP and from

$\sim$0.05 to $\sim$0.035 mW h cm^{-2} for MSP) occurs with increment in P_A (from $\sim$0.077 to $\sim$0.274 mW cm^{-2} for SCP and from $\sim$0.074 to 0.196 mW cm^{-2} for MSP), which is in agreement with previous reports.[34,35] At a particular P_A value of $\sim$0.17 mW cm^{-2}, the E_A value is higher ($\sim$0.038 mW h cm^{-2}) for $MAPbBr_3$ MSP than the corresponding value of $\sim$0.011 mW h cm^{-2} for $MAPbBr_3$ SCP, which signifies better electrochemical performance for $MAPbBr_3$ MSP.[36] The air stability of the $MAPbBr_3$ MSP based electrode was investigated over time by monitoring changes in the XRD patterns of the thick film on a glass slide. Fig. S6 (ESI†) shows the XRD patterns of the fresh and aged (7 days and 14 days) $MAPbBr_3$ MSP based electrodes stored under ambient conditions. The negligible intensity drop and broadening of the full width at half maxima (FWHM) in the aged $MAPbBr_3$ MSP based electrodes indicate high air stability of these electrodes.

Electrochemical impedance spectroscopy (EIS) was performed under 50 mV amplitude of AC voltage. A Bode modulus plot is shown in Fig. 4a where the total impedance variation with respect to frequency has been shown. At a low frequency of 0.1 Hz, the impedance reduces from 0.9 kΩ for $MAPbBr_3$ SCP to 0.66 kΩ for $MAPbBr_3$ MSP, which again confirms the reduction in the charge transfer resistances offered by the electrode–electrolyte system in MSP. The significant improvement in charge storage capacity for $MAPbBr_3$ MSP is ascribed to its higher ion-migration. Enhanced charge storage performance is observed in $MAPbBr_3$ MSP, which is evident from the frequency dependent imaginary and real capacitance plots shown in Fig. 4b and c, respectively. Frequency dependent capacitance $C(f)$ is classified into real (C_{Real}) and imaginary ($C_{Imaginary}$) counterparts revealed by the following equations:

$$C(f) = C_{Real} - jC_{Imaginary} \quad (7)$$

$$C_{Real} = -\frac{Z''}{2\pi f|Z|^2} \quad (8)$$

$$C_{Imaginary} = \frac{Z'}{2\pi f|Z|^2} \quad (9)$$

Here, Z denotes the total impedance. The variation of capacitance values with applied frequency (f) depends on the penetration of electrolyte ions from the surface into nanostructure pores. In higher frequency region, capacitive contribution comes from the surface effects only. As a consequence, lower capacitive values are obtained and capacitor mostly acted like a resistor in this region of frequency.[37] However, in the lower frequency region ($<$1 Hz) the value is enhanced as the bulk effect also resides in it. At 0.1 Hz applied frequency, the C_{Real} value remains almost constant with variation from 0.36 to 0.38 mF, whereas $\sim$38.3% enhancement in $C_{Imaginary}$ value is shown for $MAPbBr_3$ MSP ($\sim$2.38 mF) in comparison with $MAPbBr_3$ SCP ($\sim$1.72 mF). To investigate the order of ion migration inside both $MAPbBr_3$ SCP and $MAPbBr_3$ MSP, the temperature-dependent conductivity was measured under dark conditions. A thin layer of silver (Ag) was deposited on both sides of the $MAPbBr_3$ pellets to record the electrical measurements. The temperature-dependent conductivity of both the $MAPbBr_3$ pellets in the Nernst–Einstein formalism is plotted in Fig. S7 (ESI†). The ion activation energy (E_a) is derived using the Nernst–Einstein expression:[25]

$$\sigma \cdot T = \sigma_0 \exp\left(-\frac{E_a}{k_B T}\right)$$

where k_B is the Boltzman constant, T is the absolute temperature and σ_0 is a constant. From the Arrhenius plots shown in Fig. S7 (ESI†) the activation energies (E_a) of the ions are calculated to be 0.23 $\pm$ 0.07 eV and 0.21$\pm$ 0.07 eV for the $MAPbBr_3$ SCP and $MAPbBr_3$ MSP pellets, respectively. The lower E_a of $MAPbBr_3$ MSP signifies higher ion migration in comparison with the $MAPbBr_3$ SCP. In $MAPbBr_3$ MSP, the higher ion migration can accelerate the decomposition of the MSP active electrode and generate nonradiative recombination defect sites in comparison with the $MAPbBr_3$ SCP.[3,8,11] As a result, the SCP electrode shows longer stability compared to the $MAPbBr_3$ MSP electrode. On the other hand, higher ion migration of $MAPbBr_3$ MSP signifies better electrochemical performance of the $MAPbBr_3$ MSP based electrode.

Next, to understand in-depth the effect of structural evolution and layered structure on the total capacitance of LHP-based supercapacitors, three different LHPs such as 3D $MAPbBr_3$, 2D BA_2PbBr_4 and quasi-2D $BA_2MAPb_2Br_7$ were investigated. Fig. S2c and d (ESI†) show the CV spectra of BA_2PbBr_4

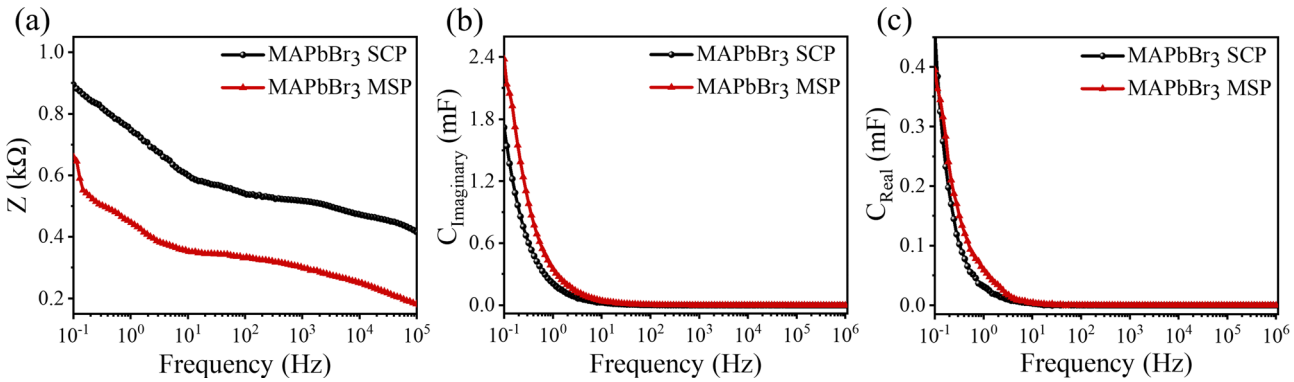

Fig. 4 (a) Total impedance, (b) imaginary part and (c) real part of capacitance are plotted with applied frequency for $MAPbBr_3$ SCP and $MAPbBr_3$ MSP electrodes.

and $BA_2MAPb_2Br_7$ MSP-based electrodes at different scan rates. The maximum areal/specific capacitance values for BA_2PbBr_4 and $BA_2MAPb_2Br_7$ MSP based electrodes are 209 mF cm^{-2}/148.25 F g^{-1}, and 205 mF cm^{-2}/138.35 F g^{-1} at a scan rate of 5 mV s^{-1}, which are much higher than those of all reported similar LHP based ESCs (Fig. 5a and b). The 2D BA_2PbBr_4 MSP-based electrode shows maximum areal/specific capacitance values as compared to all other electrodes at a low scan rate (Fig. 5c). This can be attributed to the possible effect of highest surface area (smallest particle size) as compared to the other MSPs, which improves the interaction between electrolyte ions and the perovskite electrode interface. From Fig. 5c, we clearly show that the areal capacitance of 2D BA_2PbBr_4 decreases gradually with an increase in the scan rate compared to the other MSP-based electrode. The faster reduction in the capacitance value of the BA_2PbBr_4 electrode is due to the slow ion migration and ineffective interaction between electrolyte ions and the perovskite electrode interface at a high scan rate.[8] On the other hand, the quasi-2D

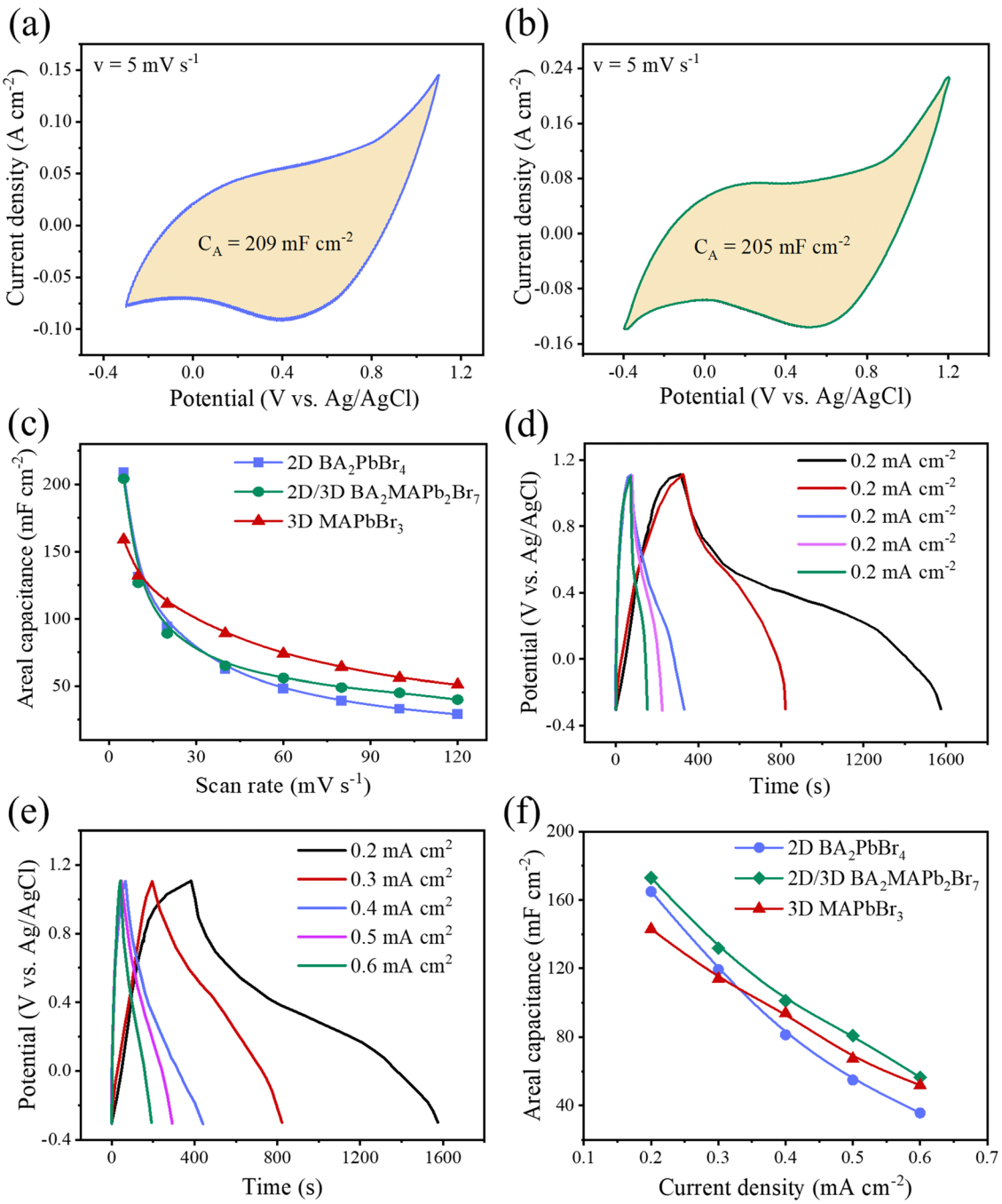

Fig. 5 CV curves at a scan rate of 5 mV s^{-1} for electrochemical cells with (a) BA_2PbBr_4 MSP and (b) $BA_2MAPb_2Br_7$ MSP electrodes. (c) Areal capacitance of electrodes (3D, 2D/3D and 2D MSP electrodes) as a function of scan rate. GCD curves of (d) BA_2PbBr_4 MSP and (e) $BA_2MAPb_2Br_7$ MSP electrodes at different current densities. (f) Areal capacitance of electrodes at different current densities.

MSP-based electrode shows higher capacitance at a higher scan rate as compared to the other MSPs. These results can be correlated to the faster interaction of the quasi-2D MSP-based electrode due to its square bar type morphological structure (Fig. S1b, ESI†). Fig. 5d and e show the GCD graphs of BA_2PbBr_4 and $BA_2MAPb_2Br_7$ MSP-based electrodes at different current densities of 0.2–0.6 mA cm^{-2}. The calculated areal/specific capacitances are 181 mF cm^{-2}/118.75 F g^{-1} for BA_2PbBr_4 MSP and 171 mF cm^{-2}/107.5 F g^{-1} for $BA_2MAPb_2Br_7$ MSP at 0.2 mA cm^{-2}, which are almost comparable. Furthermore, the variation of areal capacitance values of 2D, 3D and quasi-2D MSP electrodes with different current densities (varies from 0.2–0.6 mA cm^{-2}) is shown in Fig. 5f. All MSP electrodes show a similar trend of decreasing areal capacitance values with an increase in current density. However, the decreasing areal capacitance value with the scan rate is faster for the 2D MSP electrode due to slower charge transfer and/or ion migration with ineffective interaction at the electrolyte–electrode interface. The long-term cycling stability of BA_2PbBr_4 and $BA_2MAPb_2Br_7$ MSP based electrodes is shown in Fig. S8 (ESI†). The stability performance of the BA_2PbBr_4 SCP electrode is found to be ~98% capacitance retention, whereas the capacitance retention is around ~96% of its initial capacitance value for the $BA_2MAPb_2Br_7$ MSP electrode. However, quasi-2D MSP shows excellent capacitance values with acceptable stability among LHP MSP based electrodes, indicating the most promising alternatives for LHP based energy storage devices.

4. Conclusion

In conclusion, we have fabricated supercapacitors from powdered 2D and 3D LHPs. First, we demonstrated that the electrochemical properties of the fabricated working electrode from $MAPbBr_3$ MSP lead to the maximum specific capacitance of ~ 159 mF cm^{-2}/98.36 F g^{-1} at a scan rate of 5 mV s^{-1}, which is much higher than that of the $MAPbBr_3$ SCP and $MAPbBr_3$ based electrodes. This enhancement was attributed to the induced macrostrain, higher ionic migration and lower partial size of the $MAPbBr_3$ MSP electrode. The charge transfer resistance of the $MAPbBr_3$ MSP electrode drops to 0.66 kΩ from 0.9 kΩ for the $MAPbBr_3$ MSP electrode due to the increased ionic conductivity and specific surface area in $MAPbBr_3$ MSP. Next, three different mechanochemically synthesized bromide-based LHP (3D, 2D, and quasi-2D) based electrodes have been studied. It was found that the 2D BA_2PbBr_4 MSP based electrode shows the best performance at a low scan rate due to having the highest surface area among the electrodes, which helps to improve the interaction between electrolyte ions and perovskite electrode interface. In addition, the 2D BA_2PbBr_4 MSP based electrode has retained ~98% of its initial specific capacitance value even after 2000 GCD cycles and shows superior cyclic stability to other electrodes due to lower level of ion migration and better stability of the 2D perovskite structure. Therefore, low dimensional LHPs could be potential alternatives for developing thin-film perovskite-based supercapacitors with improved performance and stability.

Conflicts of interest

There are no conflicts to declare.

Acknowledgements

D. P. acknowledges the National Centre for Research and Development (V4-JAPAN/2/14/PeDET/2022) for financial support.

References

1 Poonam, K. Sharma, A. Arora and S. K. Tripathi, *J. Energy Storage*, 2019, **21**, 801–825.
2 P. Naskar, A. Maiti, P. Chakraborty, D. Kundu, B. Biswas and A. Banerjee, *J. Mater. Chem. A*, 2021, **9**, 1970–2017.
3 A. Mahapatra, D. Prochowicz, J. Kruszyńska, S. Satapathi, S. Akin, H. Kumari, P. Kumar, Z. Fazel, M. M. Tavakoli and P. Yadav, *J. Mater. Chem. C*, 2021, **9**, 15189–15200.
4 A. Mahapatra, D. Prochowicz, M. M. Tavakoli, S. Trivedi, P. Kumar and P. Yadav, *J. Mater. Chem. A*, 2020, **8**, 27–54.
5 G. Pacchioni, *Nat. Rev. Mater.*, 2021, **6**, 108.
6 H. Wei and J. Huang, *Nat. Commun.*, 2019, **10**, 1066.
7 A. Mahapatra, V. Anilkumar, R. D. Chavan, P. Yadav and D. Prochowicz, *ACS Photonics*, 2023, **10**, 1424–1433.
8 R. Kumar and M. Bag, *J. Phys. Chem. C*, 2021, **125**, 16946–16954.
9 R. Kumar, P. S. Shukla, G. D. Varma and M. Bag, *Electrochim. Acta*, 2021, **398**, 139344.
10 C. H. Ng, H. N. Lim, S. Hayase, Z. Zainal, S. Shafie, H. W. Lee and N. M. Huang, *ACS Appl. Energy Mater.*, 2018, **1**, 692–699.
11 L. Zhang, J. Miao, J. Li, Q. Li, L. Zhang, J. Miao, J. Li and Q. Li, *Adv. Funct. Mater.*, 2020, **30**, 2003653.
12 T. Y. Yang, G. Gregori, N. Pellet, M. Grätzel and J. Maier, *Angew. Chem., Int. Ed.*, 2015, **54**, 7905–7910.
13 W. Zhang, G. E. Eperon and H. J. Snaith, *Nat. Energy*, 2016, **1**, 16048.
14 A. Halder, M. Ghosh, A. M. Khayum, S. Bera, M. Addicoat, H. S. Sasmal, S. Karak, S. Kurungot and R. Banerjee, *J. Am. Chem. Soc.*, 2018, **140**, 10941–10945.
15 R. Kumar and M. Bag, *Energy Technol.*, 2022, **10**, 2100889.
16 S. Zhou, L. Li, H. Yu, J. Chen, C.-P. Wong, N. Zhao, S. Zhou, L. Li, H. Yu, J. Chen, C. Wong and N. Zhao, *Adv. Electron. Mater.*, 2016, **2**, 1600114.
17 R. Kumar, A. Kumar, P. S. Shukla, G. Das Varma, D. Venkataraman and M. Bag, *ACS Appl. Mater. Interfaces*, 2022, **14**, 35592–35599.
18 S. Narayanan, N. Parikh, M. M. Tavakoli, M. Pandey, M. Kumar, A. Kalam, S. Trivedi, D. Prochowicz and P. Yadav, *Eur. J. Inorg. Chem.*, 2021, 1201–1212.
19 W.-G. G. Li, H.-S. S. Rao, B.-X. X. Chen, X.-D. D. Wang and D.-B. Bin Kuang, *J. Mater. Chem. A*, 2017, **5**, 19431–19438.
20 A. Mahapatra, V. Anilkumar, J. Nawrocki, S. V. Pandey, R. D. Chavan, P. Yadav and D. Prochowicz, *Adv. Electron. Mater.*, 2023, **9**, 2300226.
21 D. Prochowicz, M. Franckevičius, A. M. Cieślak, S. M. Zakeeruddin, M. Grätzel and J. Lewiński, *J. Mater. Chem. A*, 2015, **3**, 20772–20777.

22 D. Prochowicz, P. Yadav, M. Saliba, M. Saski, S. M. Zakeeruddin, J. Lewiński and M. Grätzel, *ACS Appl. Mater. Interfaces*, 2017, **9**, 28418–28425.
23 D. Prochowicz, P. Yadav, M. Saliba, D. J. Kubicki, M. M. Tavakoli, S. M. Zakeeruddin, J. Lewiński, L. Emsley and M. Grätzel, *Nano Energy*, 2018, **49**, 523–528.
24 D. Prochowicz, M. Saski, P. Yadav, M. Grätzel and J. Lewiński, *Acc. Chem. Res.*, 2019, 3233–3243.
25 A. Mahapatra, N. Parikh, H. Kumari, M. K. Pandey, M. Kumar, D. Prochowicz, A. Kalam, M. M. Tavakoli and P. Yadav, *J. Appl. Phys.*, 2020, **127**, 185501.
26 Y. Li, L. Chen, B. Liu, P. Jin, R. Gao, L. Zhou, P. Wan, Q. Xu and X. Ouyang, *J. Mater. Chem. C*, 2021, **9**, 17124–17128.
27 Y. H. Chang, J. C. Lin, Y. C. Chen, T. R. Kuo and D. Y. Wang, *Nanoscale Res. Lett.*, 2018, **13**, 1–7.
28 D. Ghosh, K. Marjit, G. Ghosh, S. Ghosh and A. Patra, *J. Phys. Chem. C*, 2022, **34**, 14590–14597.
29 P. Muhammed Shafi and A. Chandra Bose, *AIP Adv.*, 2015, **5**, 57137.
30 K. Jayaramulu, M. Horn, A. Schneemann, H. Saini, A. Bakandritsos, V. Ranc, M. Petr, V. Stavila, C. Narayana, B. Scheibe, Š. Kment, M. Otyepka, N. Motta, D. Dubal, R. Zbořil and R. A. Fischer, *Adv. Mater.*, 2021, **33**, 2004560.
31 K. Vijaya Sankar, S. Surendran, K. Pandi, A. M. Allin, V. D. Nithya, Y. S. Lee and R. Kalai Selvan, *RSC Adv.*, 2015, **5**, 27649–27656.
32 J. Liu, J. Wang, C. Xu, H. Jiang, C. Li, L. Zhang, J. Lin and Z. X. Shen, *Adv. Sci.*, 2018, **5**, 1700322.
33 A. Kalam, R. Runjhun, A. Mahapatra, M. M. Tavakoli, S. Trivedi, H. Tavakoli Dastjerdi, P. Kumar, J. Lewiński, M. Pandey, D. Prochowicz and P. Yadav, *J. Phys. Chem. C*, 2020, **124**, 3496–3502.
34 M. Baptista, G. Gaspar, K. G. U. Wijayantha and K. Lobato, *Appl. Surf. Sci. Adv.*, 2022, **10**, 100262.
35 P. S. Chauhan, S. Kumar, A. Mondal, P. Sharma, M. N. Parekh, V. Panwar, A. M. Rao and A. Misra, *J. Mater. Chem. A*, 2022, **11**, 95–107.
36 M. I. Pratheepa and M. Lawrence, *SN Appl. Sci.*, 2020, **2**, 1–12.
37 M. Arunkumar and A. Paul, *ACS Omega*, 2017, **2**, 8039–8050.